

RADIO SOURCES FROM A 31 GHz SKY SURVEY WITH THE SUNYAEV-ZEL'DOVICH ARRAY

STEPHEN MUCHOVEJ^{1,2}, ERIK LEITCH³, JOHN E. CARLSTROM^{3,4}, THOMAS CULVERHOUSE³, CHRIS GREER³, DAVID HAWKINS¹,
RYAN HENNESSY³, MARSHALL JOY⁵, JAMES LAMB¹, MICHAEL LOH³, DANIEL P. MARRONE^{3,6}, AMBER MILLER⁷,
TONY MROCKZKOWSKI^{2,8}, CLEM PRYKE³, MATTHEW SHARP³, DAVID WOODY¹

Draft version October 30, 2018

ABSTRACT

We present the first sample of 31-GHz selected sources to flux levels of 1 mJy. From late 2005 to mid 2007, the Sunyaev-Zel'dovich Array (SZA) observed 7.7 square degrees of the sky at 31 GHz to a median rms of 0.18 mJy/beam. We identify 209 sources at greater than 5σ significance in the 31 GHz maps, ranging in flux from 0.7 mJy to ~ 200 mJy. Archival NVSS data at 1.4 GHz and observations at 5 GHz with the Very Large Array are used to characterize the sources. We determine the maximum-likelihood integrated source count to be $N(>S) = (27.2 \pm 2.5) \text{ deg}^{-2} \times (S_{\text{mJy}})^{-1.18 \pm 0.12}$ over the flux range 0.7 – 15 mJy. This result is significantly higher than predictions based on 1.4-GHz selected samples, a discrepancy which can be explained by a small shift in the spectral index distribution for faint 1.4 GHz sources. From comparison with previous measurements of sources within the central arcminute of massive clusters, we derive an overdensity of 6.8 ± 4.4 , relative to field sources.

Subject headings: techniques: interferometric, catalogs, surveys, cosmology: cosmic microwave background, cosmology: observations, radio continuum: general

1. INTRODUCTION

Until recently, prohibitive integration times have limited deep surveys at high radio frequency to small areas, or high flux cutoffs. As a result, estimates of the properties of compact extragalactic radio sources at frequencies above ~ 15 GHz have come primarily from observations at low-frequencies (in the < 10 GHz range), where the bulk of the sources are brighter, extrapolated to higher frequencies by targeted followup campaigns (de Zotti et al. 2005). While an understanding of high-frequency source populations is interesting in its own right, it is also important for the current generation of CMB and SZ experiments, many of which operate at frequencies $\gtrsim 30$ GHz, where the source population is poorly characterized.

In recent years the development of broad-band correlators has made deep surveys of significant areas of sky possible with interferometric arrays operating at 31 GHz. In this paper, we report results of a 7.7 square degree, 31-GHz sky survey with the Sunyaev-Zel'dovich Array (SZA). Although the primary goal of the SZA was to measure CMB anisotropy and to search for galaxy clusters via their Sunyaev-Zel'dovich (SZ) effect, it has also yielded the first catalog of \sim mJy sources selected at 31 GHz. This paper focuses on the results of the SZA survey observations as they pertain to the population of

high-frequency (~ 31 GHz) selected compact sources.

Several experiments, such as WMAP (Bennett et al. 2003), DASI (Kovac et al. 2002), CBI (Mason et al. 2003), and the VSA (Cleary et al. 2005), have characterized sources at 31 GHz brighter than 5 mJy. The present work extends this characterization to the fainter 31 GHz sources. As these faint sources are at or near the noise level of high-frequency CMB experiments, they represent a serious contaminant which must be carefully modeled and statistically accounted for. The OVRO/BIMA SZ group (Coble et al. 2007) have surveyed ~ 29 -GHz sources associated with massive clusters at the mJy level; the SZA survey allows a comparison of this highly-selected population with the bulk properties of field sources at 31 GHz. More recently, the CBI collaboration has followed up over 3000 1.4 GHz-selected sources at 31 GHz (Mason et al. 2009) and used these observations to predict the source population at 31 GHz. Comparison of this prediction with the SZA measurement at 31 GHz provides a direct test of the assumptions that underlie this extrapolation.

The paper is organized as follows: in §2 we present a description of the instrument and of the SZA observations. In §3 we describe follow-up observations performed with the Very Large Array (VLA), while §4 details the algorithm used to extract source fluxes from the SZA survey data. The characteristics of the 31 GHz-selected sample of sources are presented in §5, followed by a discussion in §6. Conclusions are presented in §7.

2. SUNYAEV-ZEL'DOVICH ARRAY OBSERVATIONS

2.1. *The Sunyaev-Zel'dovich Array*

The Sunyaev-Zel'dovich Array is an interferometer designed specifically for detecting and imaging the SZ effect in galaxy clusters, and is located at the Owens Valley Radio Observatory (OVRO). The SZA is equipped with an 8-GHz wideband correlator and sensitive 26-36 GHz and 85-115 GHz receivers. In this paper, we present results only from 26-36 GHz (hereafter 31 GHz) SZA observa-

arXiv:0912.2335v1 [astro-ph.CO] 11 Dec 2009

¹ California Institute of Technology, Owens Valley Radio Observatory, Big Pine, CA 93513

² Department of Astronomy, Columbia University, New York, NY 10027

³ Department of Astronomy and Astrophysics, Kavli Institute for Cosmological Physics, University of Chicago, Chicago, IL 60637

⁴ Dept. of Physics, Enrico Fermi Institute, University of Chicago, Chicago IL 60637

⁵ Space Sciences - VP62, NASA Marshall Space Flight Center, Huntsville, AL 35812

⁶ Jansky Fellow, National Radio Astronomy Observatory

⁷ Columbia Astrophysics Lab, Department of Physics, Columbia University, New York, NY

⁸ Dept. of Physics and Astronomy, U Penn, Philadelphia, PA

tions.

The SZA consists of eight 3.5-meter antennas. For the observations presented here, six were arranged in a close-packed configuration (yielding high brightness sensitivity on angular scales typical of clusters of galaxies), and two outlier antennas provided long baselines for sensitivity to compact objects. The SZA can therefore be thought of as two complementary interferometers: one with a typical resolution of a few arcminutes (short antenna separations, or *baselines*), and one with resolution of about 23 arcseconds (long baselines). For a more detailed discussion of array layout and corresponding resolution, see Muchovej et al. (2007).

In the limit where sky curvature is negligible over the instrument’s field of view, the response of an interferometer on a single baseline, known as a *visibility*, can be approximated by:

$$V(u, v) = \iint_{-\infty}^{+\infty} A(l, m) I(l, m) e^{-2\pi i\{ul+vm\}} dl dm, \quad (1)$$

where u and v are the baseline lengths projected onto the sky, l and m are direction cosines measured with respect to the (u, v) axes, $A(l, m)$ is the normalized antenna beam pattern, and $I(l, m)$ is the sky intensity distribution. Eq. 1 is a two-dimensional Fourier transform, the inverse of which is the image of the source intensity multiplied by the primary beam pattern, known as a *dirty map* I_D :

$$\begin{aligned} I_D(l, m) &\equiv A(l, m) I(l, m) \\ &= \iint_{-\infty}^{+\infty} V(u, v) e^{2\pi i\{ul+vm\}} du dv. \end{aligned} \quad (2)$$

In practice, an interferometer measures discrete Fourier modes, and structure in the dirty map is convolved with a function which reflects this incomplete Fourier-space sampling. This function, called the *synthesized beam*, is equivalent to the point-spread function for the interferometer.

It is clear from Eq. 2 that the field of view for each dirty map is limited to the size of the primary beam, $A(l, m)$, namely $\sim 11.0'$ (FWHM) for the SZA at band center (30.938 GHz). To image larger areas, we use linear mosaicking to stitch together nearby pointings which cover the region of interest (e.g., Pearson et al. 2003). Note that although large areas of sky can be surveyed in this manner, the resulting mosaics contain no information on size scales larger than that probed by the shortest baseline.

The results presented in this paper are derived from two large SZA projects: one to measure primary CMB anisotropy (Sharp et al. 2009), and the other to survey for galaxy clusters via their SZ effect. Observations were conducted differently for these two projects, as detailed in §2.3.

2.2. Field Selection

The SZA survey fields were selected to lie far from the plane of the Galaxy and to transit at high elevation at the OVRO site, minimizing atmospheric noise while optimizing the imaging capabilities of the array. Fields were spaced equally in Right Ascension (RA) to permit continuous observation. These constraints led to the selection of four regions ranging in declination from 25°

to 35° . Figure 1 depicts the approximate locations of these four fields overlaid on the IRAS 100 μm dust maps (Clegg 1980).

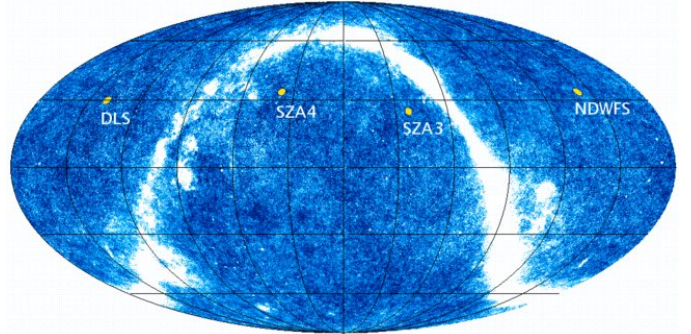


FIG. 1.— IRAS 100 μm dust map with overlay of the SZA field locations.

2.3. Observation Strategy

2.3.1. Survey Mode

Each of the four fields is split into 16 rows of 16 pointings. The pointings are equally spaced by $6.6'$ along great circles in the RA direction, and each row is equally spaced by $2.9'$ in the DEC direction. Subsequent rows are offset from one another so that the first pointing in each row is shifted by $3.3'$ in the RA direction relative to the previous row. This means that for a single field we observe an area that spans roughly 2 degrees in the RA direction and 1 degree in the DEC direction (see Figure 2).

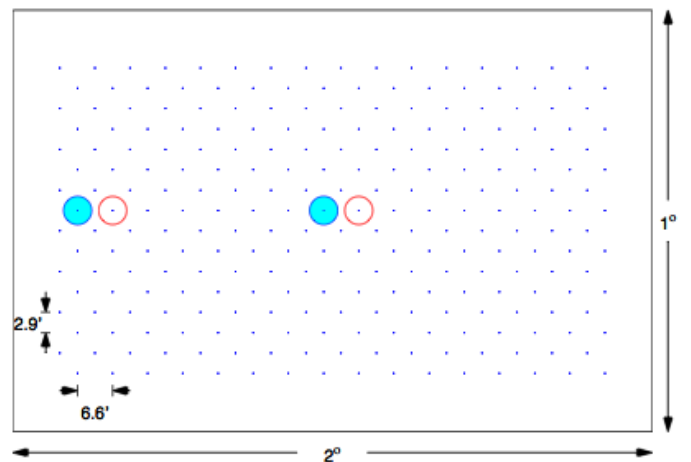


FIG. 2.— Mosaic pointing locations for a given SZA survey field. The fields are divided into 16 rows of 16 columns, with the pointings in each row separated by $6.6'$ and each row offset from each other by $2.9'$. This leads to each field being roughly 2 degrees by 1 degree in area. In a single track the SZA observed four pointings within a given row. For example, pointings in the first and ninth, followed by pointings in the second and tenth columns.

For each of the survey fields, data were taken daily in 6 hour *tracks*. In a single track, we observed two staggered pairs of pointings, all within a single row. These observations were performed in a manner that permits

ground subtraction from consecutive pointings in a pair (although ground subtraction was not used in the analysis presented here). Each track results in roughly 1 hour of observation on each of the four pointings, with very nearly the same Fourier sampling for pairs of pointings. A second track is run at a later date, with the order of the pairs reversed, to ensure that the Fourier sampling for all four pointings is comparable. In Figure 2 we show the position of the pointings in each field, and indicate how the pointings were observed in a given track.

For each set of four pointings, this sequence is repeated three times over the span of roughly one year, so that each pointing is observed in six total tracks, translating to roughly 6 hours of observation per pointing over the duration of the survey.

2.3.2. CMB anisotropy Observations

In addition to the survey observations, data were separately taken to measure the anisotropy in the CMB. These consisted of observations of 44 distinct pointings, each separated by one degree, which were not mosaicked, but analyzed individually. Of these 44 pointings, 11 overlap with pointings in the survey fields described above, and the rest are within a two degree radius of the center of the four survey fields. Where they overlap, the analysis in this paper uses the survey data only. The track structure in the anisotropy observations is similar to that in the survey analysis; see Sharp et al. (2009) for further details.

2.4. Observations

Table 1 presents details of the mosaicked SZA survey observations (see Sharp et al. (2009) for the equivalent information on the CMB anisotropy observations). The second and third columns show the approximate pointing center of each 16-row field. We also present the bandpass and gain calibrators in the next two columns, with their fluxes as measured by the SZA. In the fifth column we give the time range over which observations were taken, with the caveat that observations were not performed every day during that time span. The penultimate column lists the total unflagged integration time for data used in the analysis, and the final column gives the number of rows observed in each field. To ensure uniform coverage of all fields, tracks were repeated when necessary. Note that the full 16 rows were not observed for all fields, due to maintenance operations, instrumental characterization, and RFI monitoring. For the first 8 months of observations, the SZA4 field was used for the dedicated CMB anisotropy measurements described above. As a result, only 7 rows in the SZA4 field were completed in survey mode.

The data in the SZA survey correspond to 1493 tracks taken between November 13, 2005 and July 25, 2007. The data in the CMB anisotropy measurements correspond to an additional 414 tracks taken between November 12, 2005 and October 25, 2007. The analysis in this paper refers to the full 1907 tracks taken in both observing modes.

Data for an individual track were calibrated using a suite of MATLAB⁹ routines, which constitute a complete

pipeline for flagging, calibrating, and reducing visibility data (Muchovej et al. 2007). Although the data were reduced exactly as described in that paper, data collection differed in a few key ways: four distinct pointings were observed before observing a calibrator, and system temperature measurements were performed every eight minutes. The absolute flux calibration is referenced to Mars, assuming the Rudy (1987) temperature model, and is estimated to be accurate to better than 10%. Typical system temperatures measured throughout the survey were in the range 40-50 K. Flagging of the data as described in Muchovej et al. (2007) resulted in a loss of roughly 15% of the data. At the end of a single 6-hour track, we achieved a noise level of approximately 1.5 mJy/beam in each pointing of the short and long baseline maps.

2.5. Resulting Mosaics

Once data on all pointings in a given field are reduced, we construct a linear mosaic of the field on a regular grid of 3.3'' resolution. This scale is much less than the requirement for Nyquist sampling of the data, $\frac{1}{2D_{max}}$, where D_{max} is the longest baseline, and ensures that the number of pixels over 2 degrees is a power of 2, convenient for fast inversion of the Fourier data via FFT. The maps are a result of combining the data across our 8 GHz of bandwidth, so that they approximate the sky at the central observing frequency, 30.938 GHz. The primary beam is calculated from the Fourier transform of the aperture illumination of each telescope at the central observing frequency, modelled as a Gaussian with a central obscuration corresponding to the secondary mirror.

Unlike the maps of individual pointings, the mosaicked maps are an estimate of the true sky signal at each point in the map; that is, the taper of the primary beam has been divided out. Due to the overlap of neighboring pointings, the effective noise is approximately uniform in the interior of the mosaics, but increases significantly towards the edge of the mosaicked images. We limit the survey area by applying an edge cutoff in our mosaicked maps where the effective noise is > 0.75 mJy/beam (corresponding roughly to the one-third power point of the beam, given the noise in a single pointing).

In Table 2 we show the noise properties of the observed fields. We present the minimum and median noise (in mJy/beam) for mosaic maps made with long baselines only, short baselines only, and with the combination of the two. The median noise is calculated only in the region within which the noise is less than the 0.75 mJy/beam cutoff. The last column indicates the total area covered in each field. That the minimum and median pixel noise values are similar is an indication of the uniformity of the coverage in the survey fields. This is not the case in the CMB anisotropy fields as they consisted of discrete pointings which do not overlap on the sky.

3. VLA OBSERVATIONS

As described above, the primary goals of the SZA project were a small-scale CMB anisotropy measurement and an SZ survey for clusters of galaxies, both of which require an accurate accounting of foreground emission. Although the long and short baseline data provide some intrinsic ability to discriminate compact objects, as discussed in §2, high-sensitivity follow-up observations of

⁹ The Mathworks, Version 7.0.4 (R14), <http://www.mathworks.com/products/matlab>

TABLE 1
SURVEY OBSERVATIONS

Field Name	Field Center (J2000)		Calibrators		Dates of Observations	Integration Time (hrs)	Rows Covered
	α	δ	Bandpass (Jy) ^a	Gain (Jy) ^a			
SZA4	02 ^h 15 ^m 38 ^s .3	32°08′21″	J2253+161 (11.6)	J0237+288 (2.9)	07/11/2006 to 07/25/2007	687	7
DLS	09 ^h 19 ^m 40 ^s .0	30°01′26″	J0319+415 (11.0)	J0854+201 (5.4)	11/18/2005 to 07/06/2007	1054	14
NDWFS	14 ^h 30 ^m 08 ^s .0	35°08′34″	J1229+020 (25.3)	J1331+305 (2.1)	11/19/2005 to 07/23/2007	1000	14
SZA3	21 ^h 30 ^m 07 ^s .0	25°01′26″	J1642+398 (5.5)	J2139+143 (1.4)	11/13/2005 to 07/25/2007	1245	16

^aFluxes obtained from 31 GHz SZA observations of sources on April 16, 2006.

the SZA fields were obtained with the VLA¹⁰ to facilitate source removal.

VLA data at 1.4 GHz are publicly available from the NRAO VLA Sky Survey (NVSS; Condon et al. (1998)) for all of the SZA fields, but are limited by the relatively coarse resolution of the NVSS, 45″ FWHM, and high detection threshold of 2.5 mJy. The finer resolution (5″) and deeper sensitivity (*rms* of 0.15 mJy) obtained with the FIRST survey (White et al. 1997) are better suited for this analysis, but data are only available on half of the fields (namely the DLS and NDWFS fields).

To complement the NVSS and FIRST observations, we obtained high-sensitivity VLA observations at 5 GHz. Approximately 116 hours of observation were required to cover all four of the SZA fields, in four time blocks between 24 Feb 2007 and 15 April 2007. Data were taken at a center frequency of 4.86 GHz with the VLA D-array configuration, by mosaicking 180 pointings in each field. These pointings were arranged in 9 rows of 20 pointings in a hexagonal pattern, equally spaced by 6 arcminutes.

The pointings were mosaicked, after CLEANing, using the AIPS package FLATN, with the noise calculated using RMSD. Sources were extracted using the AIPS SAD algorithm, which iteratively removes the brightest point in a mosaic using an elliptical Gaussian model. The *rms* achieved on the VLA 5 GHz observations was roughly 70 μ Jy/beam, resulting in 859 sources from all four fields, down to a 5 σ depth of \sim 0.33 mJy. For the fields observed in CMB anisotropy mode, VLA follow-up at 8 GHz was obtained. These observations are described in Sharp et al. (2009). In this analysis, we use the VLA data to improve extraction of compact sources from our data as described in §4.

4. SOURCE EXTRACTION FROM THE SZA SURVEY

4.1. Overview

Source identification begins in the image plane, with inspection of the combined (short and long baseline) significance (*snr*) maps for the brightest pixel with significance greater than 5. Once we identify the location of a source, we next determine whether the source is extended or unresolved, as seen by the SZA or the VLA, and whether this candidate is a single source, or a collection of nearby sources. Due to the complex sidelobe structure of the synthesized beam (see §2), nearby sources must be removed simultaneously from the interferometric data; we therefore fit any additional sources within 45″ of the

primary source location, roughly twice the synthesized beam width of the long baseline maps.

Once we have determined all sources near the brightest in the map which are to be removed from the data, as well as their morphology (compact/extended), we solve for source properties by fitting to the multi-pointing visibility data. For computational expediency, we describe the sources as functions with analytic Fourier transforms (see §4.2). The best-fit models are removed from the Fourier data, and the mosaics are regenerated. This process is repeated iteratively until there are no sources brighter than 5 σ in the significance maps.

4.2. Models

When fitting sources in the mosaicked maps, we model the intensity distribution of an unresolved source as a delta function,

$$I(\nu, \vec{x}) = I_o \left(\frac{\nu}{\nu_o} \right)^{-\alpha} \delta(\vec{x} - \vec{x}_o), \quad (3)$$

where ν is the observation frequency, I_o is the intensity at frequency ν_o , defined for the SZA as the center frequency of observations, and α is the spectral index.

We model any extended source as a 2-dimensional Gaussian, i.e., up to a normalization,

$$I(\nu) \propto I_o \left(\frac{\nu}{\nu_o} \right)^{-\alpha} e^{-\frac{(l'-l_c')^2}{2\sigma_l^2}} e^{-\frac{(m'-m_c')^2}{2\sigma_m^2}}, \quad (4)$$

where l_c and m_c are the coordinates of the centroid, θ is the orientation angle, and σ_l and σ_m are the FWHM of the semi-major and semi-minor axes, respectively. In Eq. 4, the primed coordinate system (l' , m') is related to the unprimed coordinate (l , m) via a rotation by the orientation angle θ .

This model has an analytic Fourier transform provided we can take the primary beam of the SZA to be constant over the extent of the source, i.e., that the source is small compared to the primary beam. In practice, extended models are fit only to pointings within 6′ of the source, well within the FWHM of the primary beam. For a source 1′ in extent, a factor of \sim 3 larger than the most extended source in our data set, this assumption leads to an error in the fitted flux that is below 5%.

4.3. Unresolved vs. Extended Sources

Sources in the SZA maps are cross-checked against the VLA 5 GHz catalog, and a source is determined to have a counterpart at 5 GHz if a source exists within 8″ of the SZA location, a small fraction of the highest resolution element of the SZA. If a counterpart is found, we consider

¹⁰ The Very Large Array is a facility of the National Radio Astronomy Observatory, operated by Associated Universities, Inc., under a cooperative agreement with the National Science Foundation.

TABLE 2
SURVEY SENSITIVITY

Field Name	Short Baselines		Long Baselines		All Baselines		Area Covered (degree ²)
	Minimum <i>rms</i> (mJy/beam)	Median <i>rms</i> (mJy/beam)	Minimum <i>rms</i> (mJy/beam)	Median <i>rms</i> (mJy/beam)	Minimum <i>rms</i> (mJy/beam)	Median <i>rms</i> (mJy/beam)	
SZA4	0.218	0.264	0.231	0.283	0.159	0.193	0.91
DLS	0.202	0.238	0.200	0.251	0.142	0.173	1.57
NDWFS	0.219	0.239	0.219	0.249	0.156	0.172	1.56
SZA3	0.213	0.232	0.218	0.241	0.153	0.167	1.74
CMB fields	0.152	0.393	0.153	0.418	0.108	0.286	1.91

the source extended if its size at 5 GHz is greater than 22.5'' (the SZA long-baseline synthesized beam FWHM). In the rare event that the source has no 5 GHz counterpart (due presumably to source variability or resolution effects when observing extended sources) we check within 8'' of the SZA location in the 1.4 GHz NVSS or FIRST catalogs. When no counterpart is found in any of the catalogs ($\sim 3\%$ of sources), we compare the flux at that location in the short and long baseline SZA maps to determine if it is extended. If the fluxes are consistent with each other the source is classified as unresolved.

4.4. Source Location Determination

To minimize the number of degrees of freedom in each source fit, we fix the location of SZA sources with VLA counterparts to the VLA positions. We have verified that the locations of the VLA counterparts agree with locations fitted to the SZA data to within 3'', and indicate no systematic pointing offsets.

Locations are not fixed for sources determined to be extended, and for very bright sources at 31 GHz. The dynamic range (ratio of the fitted source flux to the post-fit residuals) in the mosaicked maps is approximately 35, limited by the long-term pointing accuracy of the instrument and uncertainties in the primary beam. For sources brighter than 15 mJy, however, we can fit the locations accurately in the individual pointings, resulting in an overall dynamic range in the mosaics of 70, or a factor of 2 improvement. We have verified that agreement in the fitted source location between pointings is at the arcsecond level.

4.5. Spectral Index Fitting

For source brighter than ~ 3.5 mJy, the SZA's large bandwidth allows for the simultaneous determination of the spectral index across 8 GHz. For fainter sources, however, we cannot meaningfully constrain the spectral index of the source from the SZA data alone. To reduce the number of degrees of freedom for these sources, we use the VLA 5 GHz observations (where available) as a second frequency, fixing the spectral index to

$$\alpha = -\ln(I_o/I_{5 \text{ GHz}})/\ln(\nu_o/5 \text{ GHz}) \quad (5)$$

in Eq. 3. Note that these spectral indices are used only to reduce the residuals in the maps when extracting sources. Analysis of the spectral index distribution of these sources by comparison with low-frequency data is presented in §5.3.

5. 31 GHz POPULATION CHARACTERISTICS

5.1. Source Sample

Following the procedure outlined above, we identified 209 sources at 31 GHz with *snr* greater than 5. From this sample, 40 of the sources were determined to be extended in the VLA data, yet none were seen to be resolved by the SZA, i.e. the FWHM of the fit Gaussians are all smaller than 22.5''. In Table 1 of the Appendix we present the full list of sources. The brightest source we detect has a flux of 204 mJy. Counterparts were found in the VLA 5 GHz catalog for 162 of the 171 sources with 5 GHz coverage, and 1.4 GHz NVSS counterparts were found for 157 of the 209 sources. All 1.4 GHz sources in the regions for which we have 5 GHz coverage were also found in the 5 GHz data. VLA 8 GHz coverage is available in the region for which we do not have 5 GHz coverage, and all 38 sources detected at 31 GHz in those regions have 8 GHz counterparts (Sharp et al. 2009). Of the 162 sources with 5 GHz counterparts, 34 were found to have higher fluxes at 31 GHz than at 5 GHz. In addition, 8 of the 157 sources with 1.4 GHz counterparts were found to be inverted.

5.2. Source Count

The differential source count per unit area as a function of flux, dN/dS , is typically described by a power law, i.e.,

$$\frac{dN}{dS} = N_0 \left(\frac{S}{S_0} \right)^{-\gamma}, \quad (6)$$

where N_0 is a normalization parameter per unit area, S is the source flux, and γ is the power law index. In the analysis, we take $S_0 = 1$ mJy and express the normalization as a number of sources per square degree. As models of radio source populations suggest a break in the count near 15 mJy, we fit a power-law only to sources below this limit, excluding 7 sources from the previous list. Subsequent analysis of the source count is performed on 202 sources.

5.2.1. Power law index, γ

Given a set of N_S observed source fluxes $\{S_i\}$, we can solve for the underlying population parameters by maximizing the likelihood of the dataset,

$$\mathcal{L} = \prod_i^{N_S} p(S_i | N_0, \gamma, \sigma_i), \quad (7)$$

where S_i is the observed flux of the source, and σ_i is the map noise at the source location. In the presence of noise, an observed source flux S is the combination of a "true" flux S_t and noise $N = S - S_t$. The probability in Eq. 7 can therefore be written as an integral over all

possible pairs of S_t and N that will produce an observed flux S_i :

$$p(S_i|N_0, \gamma, \sigma_i) \propto \int_0^\infty p_S(S_t|N_0, \gamma) p_N(S_i - S_t|\sigma_i) dS_t \\ \propto \int_0^\infty N_0 S_t^{-\gamma} e^{-(S_i - S_t)^2/2\sigma_i^2} dS_t, \quad (8)$$

up to a constant of proportionality (e.g., Murdoch et al. 1973). It is clear that when $p(S_i|N_0, \gamma, \sigma_i)$ is normalized, N_0 drops out of the equation. Thus, this method can only be used to calculate the power law index γ ; the *relative* frequency of sources of different flux is related only to the shape parameter γ , and is independent of the *total* number of sources. In the noiseless case, it can be trivially shown that the resulting estimator for γ meets the Fischer-Neyman criterion for a sufficient statistic, i.e., that it utilizes all the information about the shape parameter contained in the data set (e.g., Crawford et al. 1970).

In the case of non-uniform noise, the above expression leads to a normalized likelihood that depends in a complicated way on the relative areas at different noise levels in the survey. However, because our sources are selected by *snr* and not flux, it is convenient to transform directly into the *snr* basis, leading to an expression for the likelihood that is independent of the noise, and therefore of the relative areas at different noise levels:

$$p(s_i|\gamma) \propto \int_0^\infty s_t^{-\gamma} e^{-(s_i - s_t)^2/2} ds_t, \quad (9)$$

where $s \equiv S/\sigma$. We note in passing that while the kernel of Eq. 9 formally diverges as $s_t \rightarrow 0$, this is merely an artifact of the implicit assumption that the single-source hypothesis dominates the probability, i.e., that we are considering only sources well above the confusion limit. This assumption is consistent with the results quoted in §5.2.3, which indicate that the weakest source flux included in the analysis is approximately 14 times the confusion limit. In practice, we truncate Eq. 9 at an s_t which corresponds to a flux well above the confusion limit at the lowest map noise, and below which the kernel contributes negligibly to the integral.

We estimate the uncertainty in the calculated value of γ by using a quadratic approximation of the likelihood about its maximum. We have verified through extensive simulation that this method produces an unbiased estimate of the power law parameter γ and its associated uncertainty σ_γ .

5.2.2. Normalization, N_0

We can invoke Bayes' theorem to write the likelihood of a set of parameters $\{N_0, \gamma\}$ given the data D as

$$p(N_0, \gamma|D) \propto p(D|N_0, \gamma) p(N_0, \gamma) \\ \propto p(D|N_0, \gamma) p(N_0) p(\gamma). \quad (10)$$

Assuming a uniform prior for N_0 , $p(N_0) = \text{const}$, and integrating over γ , we have

$$p(N_0|D) \propto \int p(D|N_0, \gamma) p(\gamma) d\gamma. \quad (11)$$

The distribution $p(\gamma)$ is just the likelihood derived in the last section, or for computational convenience, its

Gaussian approximation. The probability of the data given N_0 and γ is the Poisson probability of the observed number of sources N_S , given the expected number of sources $\lambda(N_0, \gamma)$,

$$p(D|N_0, \gamma) \propto \frac{e^{-\lambda} \lambda^{N_S}}{N_S!},$$

where $\lambda(N_0, \gamma)$ is derived by integrating dN/dS over the noise mask of the SZA survey (given in Table 2 of the Appendix). The maximum likelihood estimate of the normalization is then just the value of N_0 that maximizes $p(N_0|D)$.

5.2.3. Results

Placing a significance cutoff on the source detections at 5σ , the source count follows a power law with $\gamma = 2.18 \pm 0.12$, and a normalization at 1 mJy of $N_0 = 32.1 \pm 3.0 \text{ deg}^{-2}$ (in the 0.7 – 15 mJy range). Integrating Equation 6 with these parameters yields an integrated source count of

$$N(>S) = (27.2 \pm 2.5) \text{ deg}^{-2} \times (S_{\text{mJy}})^{-1.18 \pm 0.12} \quad (12)$$

As discussed in §2.5, the effective noise in the interior of the mosaicked maps is nearly uniform, but increases rapidly towards the edges. Because of this nonuniformity, the 5σ significance threshold used to select sources independent of noise level does not translate simply into a uniform completeness limit across the full area of the survey. From the noise distribution, the sample is expected to be 98% complete above 1.4 mJy over a 4.3 square degree area, but 98% complete above 5 mJy over the full 7.7 square degree area. Here, we define the 98% completeness limit as the flux above which the probability of missing a source due to noise fluctuations is $< 2\%$.

5.3. Spectral Index Distribution

We calculate spectral indices for all sources in the sample (including those brighter than 15 mJy) with counterparts in the 5 GHz or 1.4 GHz VLA catalogs, where the spectral index α is defined as in Eq. 3. For each source, we construct the probability distribution for the spectral index by sampling from the flux distributions at each frequency. In the presence of noise, the conditional probability of the “true” 31 GHz flux S_t , given an observed flux S is

$$p(S_t|S, \gamma, \sigma) \propto p_S(S_t|\gamma) p_N(S - S_t|\sigma), \quad (13)$$

which is just the kernel of Eq. 8. For $\gamma > 0$, $p_S(S_t|\gamma)$ increases as $S_t \rightarrow 0$, and the observed flux S is therefore generally “boosted” by the presence of noise. Marginalizing this kernel over γ using the likelihood derived in §5.2.1 yields the distribution of S_t . For the VLA fluxes, no correction for boosting has been made. This process is repeated for each source, and the resulting probabilities are co-added to form the spectral index distribution for all sources with counterparts.

By correlating with the NVSS catalog, as described in §4.3, we find 7 instances where the higher resolution of the SZA and VLA 5 GHz data, compared to NVSS, results in the detection of two sources associated with a single NVSS source. When calculating 1.4/31 GHz spectral indices, we treat these seven pairs as a single

source. As a result, we calculate 1.4/31 GHz for 150 out of 202 sources, shown in the top panel of Figure 3. The distribution peaks at a spectral index of $\alpha \sim 0.7$, consistent with standard synchrotron emission, as expected for most sources bright at 1.4 GHz. We note that of the sources with 1.4 GHz counterparts, approximately 5% are inverted, i.e., have $\alpha < 0$. Accounting for sources undetected at 1.4 GHz will likely increase this fraction. For these sources, we use the NVSS completeness limit (~ 3.5 mJy) to construct upper limits for their spectral indices. Figure 3 illustrates the shift toward more inverted spectral indices when these limits are included.

We repeat the same calculation with the 162 sources with 5 GHz counterparts, noting that only 171 of the 209 sources are covered by the 5 GHz follow-up. The resulting spectral index distribution for these 162 sources is shown in the bottom panel of Figure 3. The distribution peaks at a value of $\alpha \sim 0.8$. Of these 162 sources, we find that 14% are inverted. Incorporating limits ($S_{5 \text{ GHz}} \sim 0.33$ mJy) for nine sources which were not detected at 5 GHz has a minimal effect on the distribution, shifting it marginally towards more inverted sources.

We stress that information about the intrinsic spectral index distribution of this population of sources can only be inferred from the observed distributions by properly accounting for the selection thresholds at each frequency. For example, we can find particular choices of intrinsic spectral index distribution that reproduce both distributions shown in Figure 3 (though in general we have no reason to expect a single distribution to describe both the 1.4/31 and 5/31 GHz spectral indices). We therefore refrain from drawing any conclusions about frequency evolution in spectral indices from these data.

6. DISCUSSION

In Figure 4, we plot the SZA dN/dS measurement over the range 0.7 – 15 mJy. In the top panel of the figure, we show results from 31 GHz-selected sources reported by OVRO/BIMA (Coble et al. 2007), CBI (Mason et al. 2003), DASI (Kovac et al. 2002), and the VSA (Cleary et al. 2005). In the bottom panel we plot the projection from de Zotti et al. (2005), and from Mason et al. (2009), based on targeted 31-GHz followup of a 1.4 GHz-selected sample of sources from the NVSS catalog.

6.1. Comparison with Cluster Source Measurements

The only prior measurement of 31-GHz selected sources complete to a comparable flux level is the Coble et al. (2007) sample of ~ 100 sources brighter than 1 mJy, found serendipitously in targeted observations of massive clusters of galaxies. Since the vast majority of these sources lie within the inner regions of clusters, these measurements permit a direct comparison of the cluster population with the 31-GHz field-source population (this work). By integrating the field-source count from the SZA and the cluster source count from Coble et al. (2007) over the flux range 0.7 – 15 mJy, we calculate the overdensity of radio sources within the central arcminute of clusters to be a factor 6.8 ± 4.4 , consistent with their estimate.

6.2. Comparison with Field Source Measurements

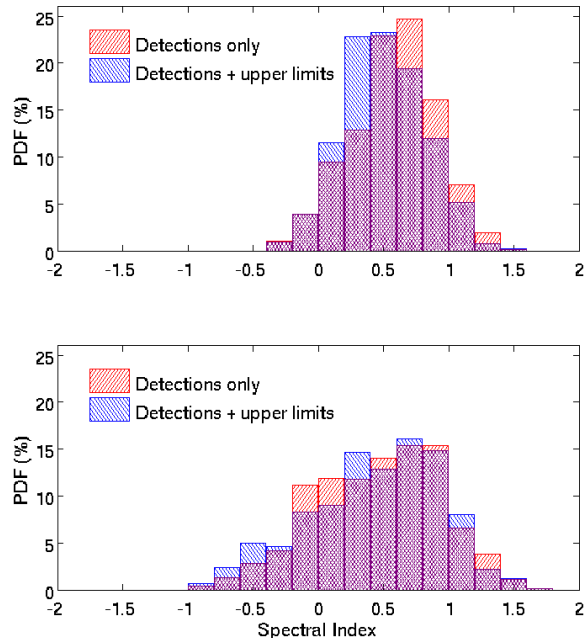


FIG. 3.— *Top*: Spectral index distribution for 31 GHz-selected sources detected with the SZA relative to their 1.4 GHz flux seen by NVSS. Red histograms denote sources with identified counterparts while blue histograms include upper limits for undetected sources, assuming the NVSS completeness limit of 3.5 mJy. *Bottom*: Same histograms but for counterparts found in the 5 GHz VLA follow-up data, with a limiting flux of 0.33 mJy at 5 GHz.

From the top panel of Figure 4, we note the general agreement between the SZA result and prior 31-GHz measurements, at the higher completeness levels of those experiments ($\gtrsim 4$ mJy). Agreement with the field-source count of Coble et al. (2007) is likewise good, although their sample in non-cluster fields consists of only four sources. From the bottom panel of Figure 4, we see that the SZA result is also consistent with the projections de Zotti et al. (2005) and Mason et al. (2009) (hereafter M09) for fluxes greater than ~ 4 mJy. At low flux, however, they deviate significantly.

The M09 projection is from a study of 3165 sources selected from the NVSS catalog at 1.4 GHz and reobserved at the same central observing frequency as the SZA. Adopting the 1.4 GHz source distribution of Hopkins et al. (2003), and an intrinsic 1.4/31 GHz spectral index distribution inferred from their own observations, they estimate the integrated 31-GHz source count over the same flux range as the SZA results to be $N(>S) = (16.7 \pm 1.7) \text{ deg}^{-2} \times (S_{mJy})^{-0.80 \pm 0.07}$. This is inconsistent with the count we determine directly at 31 GHz (§5.2.3) in both the normalization and the power law index, as shown in the bottom panel of Figure 4.

As a consistency check, we generate simulated source populations under the set of assumptions outlined in M09, apply the source extraction algorithm detailed in §4.1 to the simulated data, and apply the formalism of §5.2 to calculate the expected $N(>S)$ at 31 GHz. In particular, we generate a list of 1.4-GHz source fluxes over the range $25 \mu\text{Jy} - 1 \text{ Jy}$ using the source count of Hopkins et al. (2003), and assigning spectral indices ac-

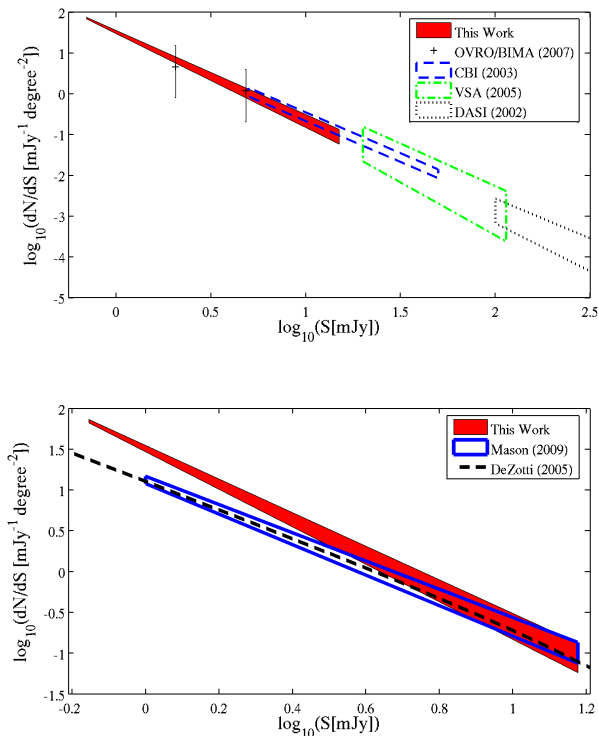


FIG. 4.— *Top*: Measurements of the 31 GHz dN/dS from this work and prior experimental results from OVRO/BIMA (Coble et al. 2007), CBI (Mason et al. 2003), the VSA (Cleary et al. 2005), and DASI (Kovac et al. 2002). *Bottom*: Comparison of the SZA dN/dS to projections from lower frequencies by de Zotti et al. (2005) and Mason et al. (2009).

cording to M09 to extrapolate these fluxes to 31 GHz. Sources are then assigned random locations on a noise map identical to the actual SZA survey coverage, with appropriate Gaussian noise added to the 31 GHz fluxes. We select only sources which would have been detected by the SZA, i.e., with snr greater than 5, and calculate the integrated source count. This procedure is repeated for 100 realizations of source populations, resulting in $N(>S) = (16.1^{+3.3}_{-2.9}) \text{ deg}^{-2} \times (S_{mJy})^{-0.86 \pm 0.18}$. This result is consistent with the prediction of M09, and demonstrates that our methodology is robust to the experimental details of the SZA survey, or differences in source selection between the two measurements.

We have also investigated whether this discrepancy can be due to differences in resolution between the SZA and the VLA in its NVSS configuration. However, of the 209 sources detected with the SZA, we note that in only 7 cases are multiple sources close enough to appear as a single source in the NVSS beam. Treating these cases as single sources, we obtain $N(>S) = (26.1 \pm 2.3) \text{ deg}^{-2} \times (S_{mJy})^{-1.19 \pm 0.13}$, an insignificant change from our nominal result (Eq. 12).

To reconcile the two measurements, we postulate a change in the 1.4/31 GHz spectral index distribution for sources below the 1.4 GHz flux limit of the M09 study. Although M09 find no significant difference between the spectral index distributions of 1.4 GHz sources with flux

> 10 mJy and sources with flux < 10 mJy, we note that their analysis is necessarily limited to sources brighter than the NVSS completeness limit of 3.5 mJy. Sources below this limit, however, constitute a large fraction of the 1.4 GHz source population used to predict the 31-GHz dN/dS , and small changes in the assumed spectral index distribution of this population can have a significant impact on the source population at 31 GHz. We note also that the SZA data suggest this hypothesis *ab initio*; while the M09 distribution predicts that fewer than 10% of sources detected by the SZA at 31 GHz would lack 1.4 GHz counterparts > 3.5 mJy, fully 25% of SZA sources lack counterparts in the NVSS catalog.

To test this hypothesis, we repeat the simulations described above, using the M09 spectral index distribution for sources above the NVSS completeness limit (3.5 mJy), and a separate spectral index distribution for sources with 1.4 GHz fluxes below 3.5 mJy. For the dim sources, we assume a distribution whose shape is identical to that of M09, but shifted with respect to it. A good match to our data can be obtained by shifting the M09 spectral distribution by 0.35 to more inverted spectra, resulting in a predicted $N(>S) = (25.5 \pm 2.9) \text{ deg}^{-2} \times (S_{mJy})^{-1.06 \pm 0.14}$. This distribution has a peak spectral index of ~ 0.7 , and predicts that $\sim 7\%$ of dim sources are inverted between 1.4 and 31 GHz. This ad hoc model also accounts for the observed fraction of SZA sources that fall below the NVSS detection threshold. In addition, this model provides a better fit than the single-component model to the observed 1.4/31 GHz spectral index distribution shown in Figure 3. Note that while this ansatz agrees well with our data, a physically motivated model of faint source spectra is likely to be much more complex.

Followup studies of faint 1.4-GHz sources at higher frequency have indeed found evidence for a flattening of the spectral index distribution near the mJy level. Prandoni et al. (2006) find that for sources whose 1.4 GHz flux is greater than 4 mJy, no sources are inverted between 1.4 and 5 GHz, but that for sources dimmer than 4 mJy at 1.4 GHz, roughly 10% of sources are inverted, comparable to the fraction of inverted sources we find between 1.4 and 31 GHz. In addition, the study of Donnelly et al. (1987) conclude that the median 1.4/5 GHz spectral index is roughly 0.75 down to a 1.4 GHz flux of 0.25 mJy, and that the fraction of flat spectrum sources increases from 22% at > 0.5 mJy to 41% in the 0.25 – 0.5 mJy range.

7. CONCLUSIONS

We present a sample of 31 GHz-selected sources from a 7.7 square degree survey obtained with the Sunyaev-Zel'dovich Array. We identify 209 sources at $> 5\sigma$ detection significance, ranging in flux from 0.7 – 204 mJy. A maximum likelihood determination of the integrated source count results in $N(>S) = (27.2 \pm 2.5) \text{ deg}^{-2} \times (S_{mJy})^{-1.18 \pm 0.12}$ in the flux range 0.7 – 15 mJy. Comparison with a measurement of 31 GHz sources towards massive galaxy clusters leads to an overdensity of 6.8 ± 4.4 , for sources within the central arcminute of massive clusters, relative to field sources.

Of the existing source samples selected at 31 GHz, the SZA sample represents the only unbiased study of sources

valid to < 1 mJy. This sample will therefore be useful in refining source models that are currently constrained by measurements at much higher flux. Since sources are also the most significant foreground for small-scale temperature anisotropy experiments, these data will be useful for the accurate inference of cosmological information from the current generation of centimeter-wave CMB anisotropy and SZ cluster survey measurements.

We thank John Cartwright, Ben Reddall and Marcus Runyan for their significant contributions to the construction and commissioning of the SZA instrument. We thank the staff of the Owens Valley Radio Observatory and CARMA for their outstanding support. We thank Jonathan Sievers and Brian Mason for helpful discussions, Bryan Butler, Claire Chandler, Gustaaf van Moorsel, and Meri Stanley for their assistance with

EVLA mosaicking observations, and Bryan Butler and Mark Gurwell for providing the Mars model to which the SZA data are calibrated. We gratefully acknowledge the James S. McDonnell Foundation, the National Science Foundation and the University of Chicago for funding to construct the SZA. The operation of the SZA is supported by NSF Division of Astronomical Sciences through grant AST-0604982. Partial support is provided by NSF Physics Frontier Center grant PHY-0114422 to the Kavli Institute of Cosmological Physics at the University of Chicago, and by NSF grants AST-0507545 and AST-05-07161 to Columbia University. AM acknowledges support from a Sloan Fellowship, and SM from an NSF Astronomy and Astrophysics Fellowship, and CG, SM, and MS from NSF Graduate Research Fellowships.

Facilities: SZA, VLA

REFERENCES

- Bennett, C. L., Hill, R. S., Hinshaw, G., Nolta, M. R., Odegard, N., Page, L., Spergel, D. N., Weiland, J. L., Wright, E. L., Halpern, M., Jarosik, N., Kogut, A., Limon, M., Meyer, S. S., Tucker, G. S., & Wollack, E. 2003, *ApJS*, 148, 97
- Cleary, K. A., Taylor, A. C., Waldram, E., Battye, R. A., Dickinson, C., Davies, R. D., Davis, R. J., Genova-Santos, R., Grainge, K., Jones, M. E., Kneissl, R., Pooley, G. G., Rebolo, R., Rubiño-Martín, J. A., Saunders, R. D. E., Scott, P. F., Slosar, A., Titterton, D., & Watson, R. A. 2005, *MNRAS*, 360, 340
- Clegg, P. E. 1980, *Phys. Scr.*, 21, 678
- Coble, K., Bonamente, M., Carlstrom, J. E., Dawson, K., Hasler, N., Holzzapfel, W., Joy, M., La Roque, S., Marrone, D. P., & Reese, E. D. 2007, *AJ*, 134, 897
- Condon, J. J., Cotton, W. D., Greisen, E. W., Yin, Q. F., Perley, R. A., Taylor, G. B., & Broderick, J. J. 1998, *AJ*, 115, 1693
- Crawford, D. F., Jauncey, D. L., & Murdoch, H. S. 1970, *ApJ*, 162, 405
- de Zotti, G., Ricci, R., Mesa, D., Silva, L., Mazzotta, P., Toffolatti, L., & González-Nuevo, J. 2005, *A&A*, 431, 893
- Donnelly, R. H., Partridge, R. B., & Windhorst, R. A. 1987, *ApJ*, 321, 94
- Hopkins, A. M., Afonso, J., Chan, B., Cram, L. E., Georgakakis, A., & Mobasher, B. 2003, *AJ*, 125, 465
- Kovac, J. M., Leitch, E. M., Pryke, C., Carlstrom, J. E., Halverson, N. W., & Holzzapfel, W. L. 2002, *Nature*, 420, 772
- Mason, B. S., Pearson, T. J., Readhead, A. C. S., Shepherd, M. C., Sievers, J., Udomprasert, P. S., Cartwright, J. K., Farmer, A. J., Padin, S., Myers, S. T., Bond, J. R., Contaldi, C. R., Pen, U., Prunet, S., Pogosyan, D., Carlstrom, J. E., Kovac, J., Leitch, E. M., Pryke, C., Halverson, N. W., Holzzapfel, W. L., Altamirano, P., Bronfman, L., Casassus, S., May, J., & Joy, M. 2003, *ApJ*, 591, 540
- Mason, B. S., Weintraub, L., Sievers, J., Bond, J. R., Myers, S. T., Pearson, T. J., Readhead, A. C. S., & Shepherd, M. C. 2009, *ApJ*, 704, 1433
- Muchovej, S., Mroczkowski, T., Carlstrom, J. E., Cartwright, J., Greer, C., Hennessy, R., Loh, M., Pryke, C., Reddall, B., Runyan, M., Sharp, M., Hawkins, D., Lamb, J. W., Woody, D., Joy, M., Leitch, E. M., & Miller, A. D. 2007, *ApJ*, 663, 708
- Murdoch, H. S., Crawford, D. F., & Jauncey, D. L. 1973, *ApJ*, 183, 1
- Pearson, T. J., Mason, B. S., Readhead, A. C. S., Shepherd, M. C., Sievers, J. L., Udomprasert, P. S., Cartwright, J. K., Farmer, A. J., Padin, S., Myers, S. T., Bond, J. R., Contaldi, C. R., Pen, U.-L., Prunet, S., Pogosyan, D., Carlstrom, J. E., Kovac, J., Leitch, E. M., Pryke, C., Halverson, N. W., Holzzapfel, W. L., Altamirano, P., Bronfman, L., Casassus, S., May, J., & Joy, M. 2003, *ApJ*, 591, 556
- Prandoni, I., Parma, P., Wieringa, M. H., de Ruiter, H. R., Gregorini, L., Mignano, A., Vettolani, G., & Ekers, R. D. 2006, *A&A*, 457, 517
- Sharp, M. K., Marrone, D. P., Carlstrom, J. E., Culverhouse, T., Greer, C., Hawkins, D., Hennessy, R., Joy, M., Lamb, J., Leitch, E., Loh, M., Miller, A. D., Mroczkowski, T., Muchovej, S., Pryke, C., & Woody, D. 2009, *ArXiv e-prints*
- White, R. L., Becker, R. H., Helfand, D. J., & Gregg, M. D. 1997, *ApJ*, 475, 479

APPENDIX

TABLE 1
SZA 30 GHz SOURCES

α (J2000)	δ (J2000)	$S_{t,31\text{ GHz}}^a$ (mJy)	$S_{31\text{ GHz}}^b$ (mJy)	snr^c	$S_{5\text{ GHz}}^d$ (mJy)	$S_{1.4\text{ GHz}}^e$ (mJy)
09:16:37.50	29:50:35.53	$14.60^{+0.15}_{-0.19}$	14.60	93.80	31.0	51.1
09:18:01.17	30:01:28.00	$8.70^{+0.15}_{-0.17}$	8.70	55.13	32.0	93.7
09:21:30.36	30:06:01.78	$6.43^{+0.17}_{-0.18}$	6.44	37.54	28.7	64.4
09:20:28.42	29:47:57.00	$4.38^{+0.15}_{-0.16}$	4.39	30.12	19.0	10.2

^a Flux corrected for boosting (i.e., S_t in Eq. 13). Errors do not reflect uncertainties in the absolute flux calibration

^b Best-fit flux, not accounting for boosting (i.e., S in Eq. 13).

^c Significance of detection in the composite mosaics

^d VLA 5 GHz flux. Map *rms* is $68\mu\text{Jy}/\text{beam}$

^e 1.4 GHz Flux from NVSS catalog

[†] Single source in NVSS catalog. 31 GHz fluxes were combined in the 1.4/31 GHz spectral index analysis

TABLE 1 — *Continued*

α (J2000)	δ (J2000)	$S_{t,31\text{ GHz}}^a$ (mJy)	$S_{31\text{ GHz}}^b$ (mJy)	snr^c	$S_5\text{ GHz}^d$ (mJy)	$S_{1.4\text{ GHz}}^e$ (mJy)
09:22:35.52	29:53:48.95	$4.08^{+0.14}_{-0.15}$	4.09	28.25	4.1	< 3.5
09:18:33.50	30:15:56.65	$3.64^{+0.17}_{-0.18}$	3.66	27.89	17.1	66.8 [†]
09:18:32.51	30:16:09.89	$2.45^{+0.17}_{-0.18}$	2.48	24.46	9.2	66.8 [†]
09:23:29.98	30:11:07.68	$4.58^{+0.19}_{-0.20}$	4.60	23.68	18.8	35.5
09:22:01.24	30:14:11.86	$3.75^{+0.16}_{-0.17}$	3.77	23.64	3.1	34.5
09:21:05.11	30:00:34.09	$3.44^{+0.17}_{-0.16}$	3.46	22.59	18.4	52.8
09:23:31.36	29:49:27.80	$3.29^{+0.17}_{-0.18}$	3.31	17.85	5.4	48.4 [†]
09:23:31.88	29:49:14.78	$1.54^{+0.17}_{-0.19}$	1.58	19.84	14.6	48.4 [†]
09:20:37.26	29:56:26.93	$2.53^{+0.15}_{-0.16}$	2.55	16.59	5.8	14.8
09:18:11.73	29:50:16.22	$3.12^{+0.15}_{-0.17}$	3.14	14.38	15.3	63.7
09:16:17.99	29:40:40.40	$6.08^{+0.40}_{-0.41}$	6.14	14.07	12.3	24.8
09:19:00.02	30:21:53.50	$2.41^{+0.20}_{-0.21}$	2.45	12.80	0.9	< 3.5
09:17:58.65	29:55:31.69	$1.74^{+0.15}_{-0.15}$	1.77	12.19	4.6	8.0
09:19:11.46	30:07:33.91	$1.93^{+0.17}_{-0.19}$	1.97	11.43	4.2	8.2
09:15:32.97	30:15:56.24	$2.77^{+0.26}_{-0.27}$	2.83	10.74	4.2	< 3.5
09:16:40.53	30:13:06.15	$1.85^{+0.16}_{-0.18}$	1.88	10.87	0.8	< 3.5
09:19:52.47	29:56:25.35	$1.07^{+0.15}_{-0.17}$	1.12	10.01	4.6	20.9
09:19:40.43	29:59:32.82	$1.48^{+0.16}_{-0.16}$	1.52	9.99	7.6	25.2
09:16:51.27	29:41:24.43	$3.32^{+0.34}_{-0.36}$	3.39	9.83	3.1	< 3.5
09:18:11.97	29:58:36.63	$1.36^{+0.15}_{-0.15}$	1.40	9.61	1.5	4.1
09:16:25.35	29:52:16.26	$1.11^{+0.15}_{-0.16}$	1.15	8.68	3.2	11.0
09:21:27.65	29:58:11.85	$1.46^{+0.14}_{-0.16}$	1.49	8.44	3.8	10.9
09:23:39.94	30:06:30.24	$1.74^{+0.22}_{-0.22}$	1.80	8.54	12.6	39.7
09:20:18.31	29:48:10.68	$1.10^{+0.15}_{-0.16}$	1.15	8.19	0.4	< 3.5
09:20:41.00	30:10:12.89	$1.27^{+0.16}_{-0.18}$	1.32	8.15	2.4	4.1
09:18:57.85	30:21:07.24	$1.56^{+0.19}_{-0.21}$	1.61	7.67	5.6	32.1
09:18:38.44	30:18:32.21	$1.29^{+0.17}_{-0.18}$	1.34	8.01	4.8	11.6
09:19:29.27	29:59:57.34	$1.23^{+0.15}_{-0.17}$	1.28	7.96	8.2	8.7
09:21:04.44	30:20:31.25	$1.32^{+0.17}_{-0.18}$	1.37	8.00	2.9	4.2
09:16:26.72	29:59:23.77	$1.45^{+0.15}_{-0.16}$	1.49	7.76	1.2	< 3.5
09:17:01.04	30:01:26.81	$1.57^{+0.16}_{-0.17}$	1.61	7.63	4.9	16.5
09:23:45.88	29:43:09.36	$2.48^{+0.34}_{-0.36}$	2.58	6.77	14.6	47.9
09:23:34.35	30:12:05.13	$1.45^{+0.20}_{-0.21}$	1.51	7.09	1.5	< 3.5
09:22:06.74	30:28:58.82	$4.36^{+0.66}_{-0.68}$	4.57	6.79	6.7	3.5
09:23:03.47	29:59:37.21	$0.98^{+0.15}_{-0.16}$	1.03	6.72	< 0.33	< 3.5
09:20:50.45	30:17:35.77	$1.03^{+0.16}_{-0.18}$	1.09	6.38	4.6	10.3
09:16:49.95	30:11:56.08	$0.93^{+0.17}_{-0.19}$	1.00	6.51	< 0.33	< 3.5
09:15:49.44	29:50:02.20	$0.94^{+0.16}_{-0.17}$	1.00	6.11	3.1	5.9
09:18:14.89	30:13:44.34	$0.97^{+0.16}_{-0.19}$	1.03	6.18	4.9	14.1
09:23:19.44	29:46:07.68	$0.97^{+0.18}_{-0.20}$	1.05	5.58	0.6	< 3.5
09:22:16.60	30:15:07.99	$1.04^{+0.16}_{-0.17}$	1.10	5.52	1.0	3.6
09:22:01.25	29:56:01.58	$0.76^{+0.14}_{-0.16}$	0.81	5.42	1.0	< 3.5
09:17:06.56	29:50:23.21	$0.76^{+0.16}_{-0.17}$	0.84	5.43	4.5	16.8
21:34:12.54	25:20:05.00	$100.74^{+0.39}_{-0.41}$	100.74	243.60	145.0	123.4
21:28:19.99	25:06:39.95	$13.68^{+0.17}_{-0.18}$	13.68	60.65	55.1	126.5
21:27:19.43	25:12:50.59	$4.42^{+0.17}_{-0.17}$	4.44	39.38	4.3	68.8 [†]
21:27:18.69	25:13:12.58	$3.04^{+0.16}_{-0.18}$	3.05	34.28	16.2	68.8 [†]
21:27:18.44	25:12:20.60	$1.67^{+0.17}_{-0.17}$	1.71	24.01	9.1	2.1
21:33:04.62	25:20:47.99	$6.83^{+0.18}_{-0.19}$	6.85	37.60	15.7	33.2
21:28:52.38	24:39:06.47	$8.16^{+0.23}_{-0.24}$	8.17	35.33	9.8	4.8
21:28:53.25	25:20:21.47	$3.41^{+0.17}_{-0.19}$	3.43	19.31	6.9	11.1
21:32:08.45	25:12:09.99	$2.86^{+0.15}_{-0.17}$	2.88	18.25	3.6	4.5
21:26:39.91	25:03:49.19	$2.37^{+0.16}_{-0.17}$	2.39	14.72	4.2	< 3.5
21:33:57.20	25:15:56.97	$2.82^{+0.21}_{-0.21}$	2.85	13.96	2.6	4.4
21:32:30.18	25:02:11.37	$2.07^{+0.16}_{-0.17}$	2.09	12.57	5.5	15.1
21:31:53.81	24:39:33.05	$2.39^{+0.20}_{-0.21}$	2.43	11.81	6.7	10.1
21:30:44.02	24:49:33.86	$2.05^{+0.15}_{-0.17}$	2.08	10.59	7.8	20.8
21:29:57.88	25:07:25.01	$1.53^{+0.16}_{-0.17}$	1.57	9.31	4.0	7.4
21:27:21.49	24:58:17.25	$1.55^{+0.15}_{-0.17}$	1.59	9.47	1.1	< 3.5
21:27:00.95	24:52:26.77	$1.49^{+0.15}_{-0.17}$	1.53	9.35	1.6	< 3.5
21:33:55.85	25:12:29.07	$1.92^{+0.20}_{-0.21}$	1.97	9.42	3.3	2.5
21:33:36.18	25:06:17.37	$1.38^{+0.16}_{-0.17}$	1.43	9.08	8.6	30.6
21:27:55.18	25:01:44.83	$1.38^{+0.16}_{-0.17}$	1.42	8.75	1.4	< 3.5
21:33:10.62	25:15:56.43	$1.34^{+0.16}_{-0.17}$	1.38	8.12	2.5	5.0
21:33:01.83	24:53:25.04	$1.30^{+0.16}_{-0.17}$	1.34	8.09	4.9	3.1
21:31:47.69	25:18:27.96	$1.31^{+0.16}_{-0.17}$	1.35	8.05	4.0	9.1

TABLE 1 — *Continued*

α (J2000)	δ (J2000)	$S_{t,31\text{ GHz}}^a$ (mJy)	$S_{31\text{ GHz}}^b$ (mJy)	snr^c	$S_5\text{ GHz}^d$ (mJy)	$S_{1.4\text{ GHz}}^e$ (mJy)
21:27:12.18	25:10:37.86	$1.16^{+0.16}_{-0.17}$	1.22	7.50	10.9	39.9
21:32:52.46	24:55:34.07	$1.53^{+0.16}_{-0.17}$	1.56	6.72	2.7	8.7
21:28:09.99	24:41:36.19	$1.28^{+0.18}_{-0.19}$	1.34	7.06	1.8	< 3.5
21:31:17.47	24:42:33.05	$1.00^{+0.17}_{-0.19}$	1.06	6.78	< 0.33	< 3.5
21:31:29.21	24:38:37.85	$1.34^{+0.23}_{-0.24}$	1.43	6.64	4.3	11.0
21:27:36.49	24:38:47.79	$1.49^{+0.23}_{-0.23}$	1.56	6.53	1.9	3.0
21:28:51.49	24:58:10.41	$0.97^{+0.16}_{-0.18}$	1.03	5.89	1.7	3.3
21:28:44.81	25:06:25.11	$0.99^{+0.16}_{-0.18}$	1.05	6.26	1.7	< 3.5
21:28:13.46	25:26:28.12	$1.88^{+0.35}_{-0.36}$	2.02	6.29	4.2	11.7
21:27:48.05	25:14:38.07	$0.92^{+0.16}_{-0.17}$	0.98	5.73	1.1	< 3.5
21:30:51.28	24:51:39.28	$0.80^{+0.15}_{-0.18}$	0.87	5.98	11.8	47.3
21:33:26.51	25:22:15.72	$0.92^{+0.20}_{-0.22}$	1.02	5.86	7.5	28.3
21:28:13.38	24:48:42.27	$0.91^{+0.17}_{-0.18}$	0.98	5.74	3.8	< 3.5
21:27:08.59	25:19:08.56	$0.96^{+0.18}_{-0.18}$	1.03	5.84	< 0.33	< 3.5
21:29:54.40	24:54:40.10	$0.83^{+0.15}_{-0.17}$	0.89	5.77	5.8	21.5
21:27:22.57	24:52:52.14	$0.95^{+0.16}_{-0.18}$	1.01	5.79	< 0.33	< 3.5
21:30:30.76	25:16:35.42	$0.84^{+0.16}_{-0.18}$	0.91	5.38	4.4	11.3
21:29:06.54	25:06:34.41	$0.91^{+0.16}_{-0.17}$	0.98	5.41	1.5	4.2
21:30:53.15	25:15:48.59	$1.24^{+0.16}_{-0.17}$	1.28	5.43	1.3	3.0
21:33:15.39	25:28:58.52	$3.53^{+0.74}_{-0.79}$	3.86	5.20	37.6	39.1
14:29:10.22	35:29:47.05	$20.31^{+0.15}_{-0.19}$	20.32	104.59	26.9	24.4
14:34:34.22	35:10:09.53	$14.50^{+0.32}_{-0.33}$	14.51	47.02	36.2	69.6
14:34:00.30	35:11:52.30	$8.08^{+0.17}_{-0.18}$	8.09	45.83	10.1	12.2
14:27:58.74	34:59:19.92	$6.95^{+0.17}_{-0.18}$	6.96	39.29	5.7	6.8
14:26:32.19	35:08:14.88	$5.49^{+0.16}_{-0.18}$	5.50	31.69	30.1	95.0
14:25:41.98	34:58:39.37	$5.68^{+0.31}_{-0.32}$	5.71	23.23	35.6	154.7
14:25:40.39	34:58:05.78	$7.94^{+0.34}_{-0.34}$	7.98	20.96	29.2	67.4
14:31:34.55	35:15:11.30	$2.92^{+0.16}_{-0.17}$	2.94	20.24	21.2	76.0
14:34:13.86	34:55:05.49	$3.34^{+0.18}_{-0.19}$	3.37	18.35	2.1	4.8
14:27:59.15	34:55:21.07	$3.79^{+0.17}_{-0.19}$	3.80	13.44	7.6	34.1
14:33:15.26	34:51:41.46	$3.17^{+0.21}_{-0.23}$	3.20	16.26	23.2	90.8
14:33:20.62	34:50:34.85	$1.83^{+0.25}_{-0.26}$	1.90	9.97	18.9	90.6
14:27:02.24	34:59:04.28	$2.75^{+0.17}_{-0.18}$	2.78	15.73	8.2	17.7
14:27:41.14	34:59:31.52	$2.53^{+0.17}_{-0.17}$	2.56	14.61	1.6	< 3.5
14:29:09.28	35:03:25.16	$1.70^{+0.17}_{-0.18}$	1.74	13.25	7.8	46.6 [†]
14:29:11.11	35:03:20.78	$1.08^{+0.17}_{-0.18}$	1.14	10.44	2.7	46.6 [†]
14:29:06.01	35:11:15.69	$2.30^{+0.17}_{-0.19}$	2.33	13.20	6.2	13.2
14:28:50.46	34:54:20.89	$2.41^{+0.18}_{-0.19}$	2.44	12.98	5.8	9.5
14:32:45.57	34:55:38.10	$2.11^{+0.17}_{-0.17}$	2.14	12.51	0.6	< 3.5
14:33:09.89	35:15:18.21	$1.82^{+0.17}_{-0.17}$	1.86	11.63	9.4	29.2
14:30:26.60	35:19:20.71	$3.41^{+0.16}_{-0.17}$	3.43	11.03	5.8	20.8
14:32:13.54	35:09:41.03	$1.72^{+0.16}_{-0.17}$	1.76	10.12	6.6	16.5
14:29:22.90	35:12:19.80	$1.73^{+0.17}_{-0.18}$	1.77	10.48	2.0	< 3.5
14:34:35.36	35:26:22.24	$3.01^{+0.31}_{-0.32}$	3.08	10.08	14.3	30.8
14:27:17.93	35:01:30.76	$1.75^{+0.17}_{-0.18}$	1.79	9.98	3.1	4.9
14:30:11.82	35:00:20.16	$1.80^{+0.16}_{-0.17}$	1.83	9.97	5.4	12.7
14:26:51.48	35:19:24.68	$1.59^{+0.16}_{-0.17}$	1.62	9.49	5.7	4.4
14:29:53.81	35:17:54.52	$1.92^{+0.16}_{-0.17}$	1.96	9.36	0.9	< 3.5
14:32:39.93	35:11:58.74	$1.48^{+0.17}_{-0.17}$	1.53	8.92	0.8	< 3.5
14:32:37.98	35:30:36.88	$1.79^{+0.20}_{-0.21}$	1.84	8.88	7.0	19.9
14:28:50.71	34:53:15.03	$1.72^{+0.19}_{-0.21}$	1.76	8.65	2.1	2.3
14:34:21.94	35:25:17.88	$1.64^{+0.20}_{-0.22}$	1.69	8.48	4.5	9.1
14:34:39.66	35:08:27.84	$3.43^{+0.38}_{-0.40}$	3.52	8.16	2.8	5.6
14:34:34.17	35:09:58.11	$2.22^{+0.30}_{-0.32}$	2.31	8.04	36.2	69.6
14:31:12.34	35:35:26.58	$4.12^{+0.50}_{-0.52}$	4.25	7.57	3.7	6.8
14:32:56.09	35:33:39.50	$2.25^{+0.32}_{-0.34}$	2.35	7.90	17.5	66.3
14:27:26.98	35:02:12.07	$1.26^{+0.17}_{-0.19}$	1.31	7.69	0.6	< 3.5
14:28:51.10	35:30:30.07	$1.39^{+0.20}_{-0.22}$	1.45	7.24	7.1	23.1
14:32:16.89	35:02:48.92	$1.11^{+0.18}_{-0.18}$	1.17	7.28	0.7	< 3.5
14:28:25.47	34:55:47.06	$1.08^{+0.17}_{-0.19}$	1.13	7.05	4.8	11.7
14:29:23.66	35:28:51.22	$1.26^{+0.18}_{-0.19}$	1.32	6.89	2.9	7.9
14:26:34.41	34:59:29.06	$0.87^{+0.17}_{-0.18}$	0.94	5.60	3.6	8.1
14:34:32.42	35:22:20.90	$1.53^{+0.26}_{-0.28}$	1.63	6.19	< 0.33	< 3.5
14:30:09.94	35:19:57.93	$0.90^{+0.16}_{-0.18}$	0.96	6.02	0.4	< 3.5
14:29:48.68	35:17:47.91	$1.03^{+0.17}_{-0.17}$	1.09	6.12	5.2	15.2
14:29:05.66	34:49:10.32	$1.84^{+0.34}_{-0.38}$	1.98	5.82	11.7	33.4

TABLE 1 — *Continued*

α (J2000)	δ (J2000)	$S_{t,31\text{ GHz}}^a$ (mJy)	$S_{31\text{ GHz}}^b$ (mJy)	snr^c	$S_5\text{ GHz}^d$ (mJy)	$S_{1.4\text{ GHz}}^e$ (mJy)
14:33:01.39	35:01:49.41	$0.82^{+0.16}_{-0.19}$	0.89	5.10	0.7	< 3.5
14:32:59.91	35:28:33.87	$0.85^{+0.17}_{-0.19}$	0.93	5.41	5.6	17.8
14:33:08.12	35:31:50.30	$1.34^{+0.24}_{-0.26}$	1.43	5.83	1.3	2.8
14:31:00.42	35:36:32.76	$5.35^{+0.74}_{-0.76}$	5.57	5.56	12.8	38.1
14:32:39.56	35:01:51.23	$0.85^{+0.16}_{-0.17}$	0.92	5.55	6.0	15.1
14:28:34.05	34:57:02.02	$0.84^{+0.17}_{-0.19}$	0.91	5.39	< 0.33	< 3.5
14:34:03.67	35:24:53.09	$0.82^{+0.17}_{-0.18}$	0.89	5.32	< 0.33	< 3.5
14:29:34.77	35:27:42.12	$0.78^{+0.18}_{-0.19}$	0.87	5.02	0.6	2.6
02:18:42.20	31:49:26.88	$147.47^{+0.22}_{-0.22}$	147.47	662.28	112.0	56.8
02:14:15.63	32:03:50.44	$26.83^{+0.19}_{-0.20}$	26.83	131.45	30.6	11.7
02:13:39.17	31:59:27.36	$2.37^{+0.16}_{-0.18}$	2.39	23.85	11.4	62.8^\dagger
02:13:38.65	31:59:07.72	$2.67^{+0.17}_{-0.17}$	2.69	21.09	2.2	62.8^\dagger
02:13:38.33	31:58:48.36	$2.12^{+0.17}_{-0.17}$	2.15	23.64	7.6	< 3.5
02:16:35.38	32:00:22.55	$3.26^{+0.15}_{-0.17}$	3.28	21.08	19.7	47.5
02:14:02.07	32:06:13.47	$1.90^{+0.17}_{-0.19}$	1.94	19.77	0.9	< 3.5
02:14:02.15	32:06:06.63	$1.91^{+0.18}_{-0.18}$	1.95	19.30	0.6	< 3.5
02:16:45.58	32:03:58.85	$3.20^{+0.16}_{-0.16}$	3.21	16.59	10.4	19.5
02:18:50.64	32:03:28.96	$2.68^{+0.16}_{-0.16}$	2.70	16.43	5.3	9.8
02:19:02.96	31:59:47.82	$2.11^{+0.16}_{-0.17}$	2.14	10.50	9.8	27.5
02:13:55.80	31:52:59.74	$1.86^{+0.17}_{-0.18}$	1.89	10.36	3.7	10.0
02:15:19.89	31:52:42.50	$1.66^{+0.18}_{-0.20}$	1.71	9.53	8.9	19.1
02:16:01.36	31:48:22.72	$2.56^{+0.29}_{-0.30}$	2.63	9.23	8.7	12.7
02:17:53.59	31:50:14.93	$1.69^{+0.21}_{-0.20}$	1.75	8.84	1.5	< 3.5
02:12:56.83	32:02:22.54	$1.34^{+0.16}_{-0.17}$	1.39	8.41	2.7	5.7
02:14:09.72	32:06:39.97	$0.86^{+0.19}_{-0.20}$	0.95	7.00	3.9	24.5
02:13:31.80	31:58:08.46	$1.10^{+0.16}_{-0.17}$	1.16	6.84	0.4	< 3.5
02:12:43.34	31:58:56.93	$0.96^{+0.16}_{-0.18}$	1.02	5.76	4.3	9.6
02:15:53.67	32:03:03.79	$1.01^{+0.16}_{-0.18}$	1.07	6.21	1.7	3.0
02:17:19.14	31:58:11.28	$0.80^{+0.18}_{-0.17}$	0.88	5.42	—	< 3.5
02:18:02.31	32:02:59.07	$0.79^{+0.16}_{-0.18}$	0.87	5.11	—	< 3.5
02:22:48.81	33:57:19.00	$12.35^{+0.13}_{-0.15}$	12.35	87.84	—	189.3
02:22:22.79	34:00:15.65	$5.63^{+0.51}_{-0.52}$	5.74	10.98	—	5.5
02:22:46.21	34:04:33.89	$1.39^{+0.31}_{-0.34}$	1.54	5.18	—	15.1
02:30:41.98	33:56:21.46	$4.02^{+0.34}_{-0.20}$	4.04	20.28	—	35.3
02:11:40.54	33:04:17.31	$2.59^{+0.30}_{-0.32}$	2.67	8.56	—	21.4
02:20:45.66	32:57:05.64	$3.13^{+0.24}_{-0.24}$	3.18	8.50	—	23.5
02:24:36.11	32:51:45.89	$4.43^{+0.30}_{-0.31}$	4.48	14.09	—	8.5
02:16:03.95	33:03:45.08	$1.03^{+0.21}_{-0.23}$	1.12	5.27	—	< 3.5
02:20:48.03	32:41:06.53	$204.05^{+0.47}_{-0.49}$	204.05	417.06	—	921.6
02:20:17.28	32:38:53.09	$4.28^{+0.26}_{-0.27}$	4.32	16.28	10.1	10.2
02:25:00.23	32:31:36.95	$7.41^{+0.36}_{-0.36}$	7.45	20.48	—	16.8
02:24:40.90	32:29:39.65	$1.21^{+0.27}_{-0.29}$	1.33	5.16	—	< 3.5
02:24:27.44	32:34:27.52	$0.83^{+0.13}_{-0.14}$	0.87	4.72	—	2.3
02:11:48.05	32:09:32.41	$1.20^{+0.26}_{-0.28}$	1.32	5.05	—	< 3.5
02:20:24.90	32:10:45.30	$1.45^{+0.11}_{-0.13}$	1.46	11.18	7.3	17.5
02:20:11.45	32:10:42.50	$1.46^{+0.19}_{-0.21}$	1.52	6.36	5.9	19.7
02:24:40.70	32:02:05.45	$6.20^{+0.33}_{-0.33}$	6.24	19.66	—	6.5
02:24:40.56	32:08:43.00	$1.25^{+0.13}_{-0.13}$	1.28	9.94	—	7.1
02:24:59.44	32:14:04.83	$2.24^{+0.28}_{-0.29}$	2.32	6.30	—	25.3
02:16:27.02	32:08:15.51	$0.76^{+0.12}_{-0.15}$	0.81	6.27	0.7	< 3.5
02:16:28.14	32:10:30.20	$0.62^{+0.12}_{-0.14}$	0.67	5.48	1.6	3.4
14:18:40.52	35:30:02.51	$6.82^{+0.14}_{-0.15}$	6.82	47.72	—	91.5^\dagger
14:18:40.59	35:30:23.21	$0.85^{+0.16}_{-0.17}$	0.91	5.88	—	91.5^\dagger
14:18:40.27	35:29:41.86	$2.53^{+0.21}_{-0.21}$	2.57	10.89	—	< 3.5
14:18:40.86	35:33:24.71	$1.38^{+0.18}_{-0.18}$	1.44	8.22	—	27.4
14:22:54.68	35:32:08.97	$0.72^{+0.14}_{-0.16}$	0.78	5.28	—	3.4
14:22:42.74	35:31:48.44	$0.68^{+0.15}_{-0.17}$	0.75	5.05	—	4.5
21:24:22.68	24:55:12.95	$8.72^{+0.30}_{-0.31}$	8.74	29.65	—	4.5
21:24:32.61	25:03:17.39	$1.75^{+0.32}_{-0.34}$	1.87	5.31	—	5.8
14:22:38.77	34:58:18.65	$1.37^{+0.24}_{-0.26}$	1.47	6.00	—	< 3.5
21:25:03.78	25:25:12.85	$4.58^{+0.54}_{-0.56}$	4.72	8.56	—	< 3.5
21:24:34.23	25:27:58.04	$0.98^{+0.19}_{-0.20}$	1.06	4.41	—	7.4
02:11:43.10	33:31:39.73	$4.27^{+0.21}_{-0.23}$	4.29	19.54	—	12.6
02:11:31.56	33:23:02.49	$4.22^{+0.28}_{-0.30}$	4.26	14.80	—	< 3.5
02:19:30.26	33:28:51.69	$57.66^{+0.29}_{-0.26}$	57.67	224.25	—	100.7
02:19:43.75	33:30:28.66	$1.17^{+0.20}_{-0.22}$	1.25	6.10	—	< 3.5

TABLE 1 — *Continued*

α (J2000)	δ (J2000)	$S_{t,31\text{ GHz}}^a$ (mJy)	$S_{31\text{ GHz}}^b$ (mJy)	snr^c	$S_5\text{ GHz}^d$ (mJy)	$S_{1.4\text{ GHz}}^e$ (mJy)
02:24:23.34	33:32:30.01	$3.23^{+0.29}_{-0.30}$	3.29	11.45	—	18.3
02:23:33.81	33:24:35.41	$3.91^{+0.60}_{-0.62}$	4.11	6.77	—	54.5
21:24:50.28	26:01:50.36	$7.85^{+0.19}_{-0.20}$	7.86	33.37	—	8.6 [†]
21:24:50.34	26:01:59.06	$1.85^{+0.21}_{-0.22}$	1.91	8.50	—	8.6 [†]
21:33:02.14	26:04:17.99	$1.32^{+0.29}_{-0.32}$	1.46	5.24	—	< 3.5
21:36:42.22	25:57:41.47	$15.21^{+0.50}_{-0.52}$	15.24	28.20	—	10.4
21:36:55.58	25:56:43.63	$4.38^{+0.30}_{-0.31}$	4.42	14.43	—	6.1

TABLE 2
SZA AREA COVERAGE

Noise Value (mJy)	\sum Area (deg ²)
0.11	0.000
0.12	0.014
0.13	0.037
0.14	0.080
0.15	0.219
0.16	0.638
0.17	2.578
0.18	3.629
0.19	4.012
0.20	4.281
0.21	4.504
0.22	4.697
0.23	4.868
0.24	5.023
0.26	5.323
0.28	5.554
0.30	5.758
0.32	5.940
0.34	6.106
0.36	6.257
0.38	6.396
0.40	6.525
0.45	6.807
0.50	7.036
0.55	7.226
0.60	7.385
0.65	7.514
0.70	7.613
0.75	7.684